Applied Surface Science 408 (2017) 117–124

Contents lists available at ScienceDirect

Applied Surface Science

journal homepage: www.elsevier.com/locate/apsusc

Full Length Article

Cu-Ni nanowire-based TiO_2 hybrid for the dynamic photodegradation of acetaldehyde gas pollutant under visible light

Shuying Zhu[a,b], Xiaofeng Xie[a,*], Sheng-Chieh Chen[c], Shengrui Tong[d], Guanhong Lu[a], David Y.H. Pui[c], Jing Sun[a]

[a] Shanghai Institute of Ceramics, Chinese Academy of Sciences, Shanghai 200050, China
[b] University of Chinese Academy of Sciences, 19 Yuquan Road, Beijing 100049, China
[c] College of Science and Engineering, University of Minnesota, Minneapolis, MN 55455, USA
[d] Institute of Chemistry, Chinese Academy of Sciences, Beijing 100190, China

ARTICLE INFO

Article history:
Received 3 February 2017
Received in revised form 24 February 2017
Accepted 25 February 2017
Available online 1 March 2017

Keywords:
Photocatalysis
Cu-Ni bimetallic nanowire
TiO_2
Acetaldehyde
Dynamic photodegradation

ABSTRACT

One-dimensional bimetallic nanowires were introduced into TiO_2-based matrix to enhance their photocatalysis efficiency and expand their light absorption range in this work. Recently, metal nanowires have attracted many attention in photocatalyst research fields because of their favorable electronic transmission properties and especially in the aspect of surface plasmon resonance effects. Moreover, Cu-Ni bimetallic nanowires (Cu-Ni NWs) have shown better chemical stability than ordinary monometallic nanowires in our recent works. Interestingly, it has been found that Ni sleeves of the bimetallic nanowires also can modify the Schottky barrier of interface between TiO_2 and metallic conductor, so that be beneficial to the separation of photogenerated carriers in the Cu-Ni/TiO_2 network topology. Hence, a novel heterostructured photocatalyst composed of Cu-Ni NWs and TiO_2 nanoparticles (NPs) was fabricated by one-step hydrolysis approach to explore its photocatalytic performance. TEM and EDX mapping images of this TiO_2 NPs @Cu-Ni NWs (TCN) hybrid displayed that Cu-Ni NWs were wrapped by compact TiO_2 layer and retained the one-dimensional structure in matrix. In experiments, the photocatalytic performance of the TCN nanocomposite was significantly enhanced comparing to pure TiO_2. Acetaldehyde, as a common gas pollutant in the environment, was employed to evaluate the photodegradation efficiency of a series of TCN nanocomposites under continuous feeding. The TCN exhibited excellent potodegradation performance, where the dynamic photocatalytic efficiency of TCN containing 3 wt% Cu-Ni NWs was about 88% and 56% (continuous 500 ppm CH_3CHO feeding, 20 SCCM) under UV and visible light, respectively. ESR results proved that the recombination of photo-generated electron-hole pairs was inhibited significantly in TCN nanocomposite. Finally, the mechanism for electron-hole pairs' separation and transmission at Schottky barrier interface between Cu-Ni NWs and TiO_2 layers has been proposed based on the above analyses.

1. Introduction

Due to dramatic economic growth and rapid urbanization, people are moving into new built high-rise apartments and office employees are being relocated in commercial high buildings. However, it has been widely reported that volatile organic compounds (VOCs) with high concentrations were observed in the indoor environment of these new buildings, which were released mainly from new furnishings, glues, paints, etc. [1,2]. The VOCs have shown a strong correlation with lung cancer [3]. Furthermore, it has been proved that VOCs can accelerate the formation of haze pollution in outdoors through a series of heterogeneous reactions [4,5]. Hence, how to degrade VOCs effectively has drawn more and more attentions. To solve this problem, many different methods have been investigated, such as adsorption, photocatalytic oxidation, plasma catalytic oxidation, and biotechnical decomposition [6–10]. Among them, heterogeneous photocatalysis has become an attractive technology for VOCs remove, particularly due to its potential to oxidize a wide range of VOCs with relatively high degradation efficiency under moderate conditions [11–14]. Among the multiple choices of photocatalysts, TiO_2 based nanomaterials have been the most commonly employed ones because of their low-price, readily avail-

* Corresponding author.
E-mail address: xxfshcn@163.com (X. Xie).

http://dx.doi.org/10.1016/j.apsusc.2017.02.217
0169-4332/

ability, and high chemical stability [15–17]. However, the overall efficiency of photon utilization by TiO_2 is limited by its wide band gap, high electron–hole recombination, unfavorable photon scattering, and so on [18,19].

Recently, various TiO_2-based hybrid heterostructures have been fabricated, including Ag/TiO_2 [20], Cu/TiO_2 [21], graphene/TiO_2 [22,23], and SnO_2/TiO_2 [24]. From these studies, metal-TiO_2 semiconductor were often used because they can significantly increase the photocatalytic activity and light harvesting efficiencies by improving the charge separation at the interfaces between TiO_2 and metal. In addition, surface plasmon resonance (SPR) effect of metal will enhance the adsorption and spread of incident light in the near surface of TiO_2 composites [25,26]. Among all these metals, copper is the most promising metal due to its low cost, abundant resources, non-toxicity and excellent electrical conductivity. The combination of encapsulating copper particle with TiO_2 can help fetch out electrons and thus avoid recombination of photogenerated electron-holes during the light absorption as well as related photochemical processes [27,28]. Compared with nanoparticles, metal nanowires show higher efficient catalytic activity due to the exposure of more surface active atoms which enhances the catalytic chemical reactions. So researchers have been considering to utilizing metal nanowires as core material [29–31] because their one-dimensional topology can improve the electron's transmission performances.

However, the stability of copper is not satisfying under some extreme conditions, so the Cu nanowire based photocatalyst is easily to be oxidized to lose its activity [32]. To solve this problem, alloying of other stable metal such as Ni is an effective way to increase the stability of Cu [33,34]. Besides, in the aspect of metal loading, bimetallic loaded TiO_2 also exhibited better photocatalytic activities for organic oxidation than the monometallic nanoparticles loaded TiO_2 [35]. Alloying with Ni can change the surface chemical composition, crystalline and valence structures of Cu, promoting electron transfer and cross the barrier between TiO_2 and metal [36]. On the one hand, a large barrier between metal and semiconductor can enhance electron–hole separation, but on the other the higher barrier at the junction will instead prevent more electrons transferring from TiO_2 to metal, and more energy will also be needed for electrons to transfer, which suppresses the electron transfer process [37–39].

In this work, Cu-Ni NWs consisting of a Cu nanowire core and Ni shell were introduced to a metal-TiO_2 photocatalytic system. TCN composites had been successfully synthesized by a simple chemical method based on our previous work. The as-prepared photocatalysts were been evaluated by the degradation of flowing acetaldehyde gas which is a frequently used VOCs in the environment. The characters of different weight ratios of Cu-Ni NWs in the TiO_2 composites had been verified to optimize their performances. Subsequently, the mechanism for the enhanced photocatalytic activity of TCN composites had been discussed in detail.

2. Experimental

2.1. Materials

All materials and chemicals were used as acquired without further purification.

HAD (1-Hexadecylamine, 8 g) and CTAB (Cetyl Trimethyl Ammonium Bromide, 0.5 g) were mixed and melted at 180 °C to form a clear and colorless solution. Then copper acetylacetonate was added into the pre-prepared solution, and after being kept at 180 °C for 30 min, platinum nanoparticle catalysts were added to the reaction system to promote the reduction of copper ions. With the catalyst existences, copper nanowires began to form and growth with low speed. The solution was kept at 180 °C for 10 h and nickel acetate (0.2–1.3 g) was then added in the solution and the temperature rapidly increased to 210 °C. The solution was kept at this temperature for another 2 h. After being washed and dispersed by toluene, the Cu-Ni NWs were stored at room temperature.

2.2. Synthesis of TCN binary nanocomposites

Typically, the obtained black solution of Cu-Ni NWs were filtered and washed by ethanol several times, then the Cu-Ni NWs were dispersed in 100 mL ethanol by sonication for 1 h to obtain uniform and stable solutions with a high weight fraction of Cu-Ni NWs, respectively. Afterward, 5 ml of TIP (Titanium isopropylate, Sigma 97%) were added into the Cu-Ni NWs solution under continuous magnetic stirring followed by addition of 10 mL DI water, then the mixtures were kept under stirring for 1 h to complete the reaction. Afterwards the suspensions were centrifuged and washed with ethanol several times, then the precipitates were dried in vacuum oven overnight to obtain powder samples. The samples were annealed at 400 °C for 3 h in Ar atmosphere and marked as S1, S3, S5, S20 and S0, which represented the weight ratio of Cu-Ni NWs in composites were 1%, 3%, 5%, 20% and 0 respectively.

2.3. Characterization

The surface morphology and microstructures of the samples were characterized by using a field-emission scanning electron microscopy (Magellan 400) and a transmission electron microscopy (JEM-2100F) with EDS spectrometer. The crystal structures of the samples were investigated by an X-ray diffractometer (XRD; Ultima IV 2036E102, Rigaku Corporation, Japan) with Cu Ka radiation. The UV–visible absorption spectra of samples were obtained by a UV–VIS-NIR spectrophotometer (Model Cary-5000, Varian, USA) equipped with an integrating sphere assembly. Raman spectra were recorded from 65 to 1000 cm^{-1} on a DXR Raman Microscope, Thermal Scientific corporation, USA, with a 532 nm excitation length. Electron spin resonance (ESR) signals of radicals spin-trapped by 5,5-dimethyl-1-pyrroline N-oxide (DMPO) recorded on JES-FA200 spectrometer. Samples for ESR measurement were prepared by mixing the samples in a 40 mM DMPO solution tank (aqueous dispersion for DMPO–$^{\bullet}OH$ and methanol dispersion for DMPO–$^{\bullet}O_2^-$) and irradiated with visible light.

2.4. Photocatalytic activity measurement

The photocatalytic activity experiments of all TCN samples were tested by degradation of gaseous acetaldehyde in flowing mode by using on-line photocatalysis test system which combined with a SP 502 gas chromatograph (GC) equipped with a flame ionization detector and a 2 m stainless-steel column (GDX-403) at 100 °C. All the photocatalytic activity experiments were performed at ambient temperature (maintained constant by using a fan cooling system), and the relative humidity were kept at 45%. The reusability properties of the photocatalyst were further established by collecting them after the degradation reaction and washing with ethanol before reintroducing into another cycle.

The sealed photo-reactor was a 300 mL cuboid quartz vessel (20 cm × 10 cm × 1.5 cm), which consisted of an inlet, an outlet and a quartz glass cover. The catalysts were prepared by coating the suspension of TCN composites powders onto the glass plates with diameters of 12 cm × 5 cm areas homogeneously. The weight of the photocatalyst used for each experiment was kept at 0.1 g. The catalysts were dried at 80 °C for 2 h and then cooled to room temperature before use. After the photocatalysts were placed in the reactor, the acetaldehyde vapor (500 ppm) mixed with air flowed into the reactor steadily with 20 sccm flow rate. According to this

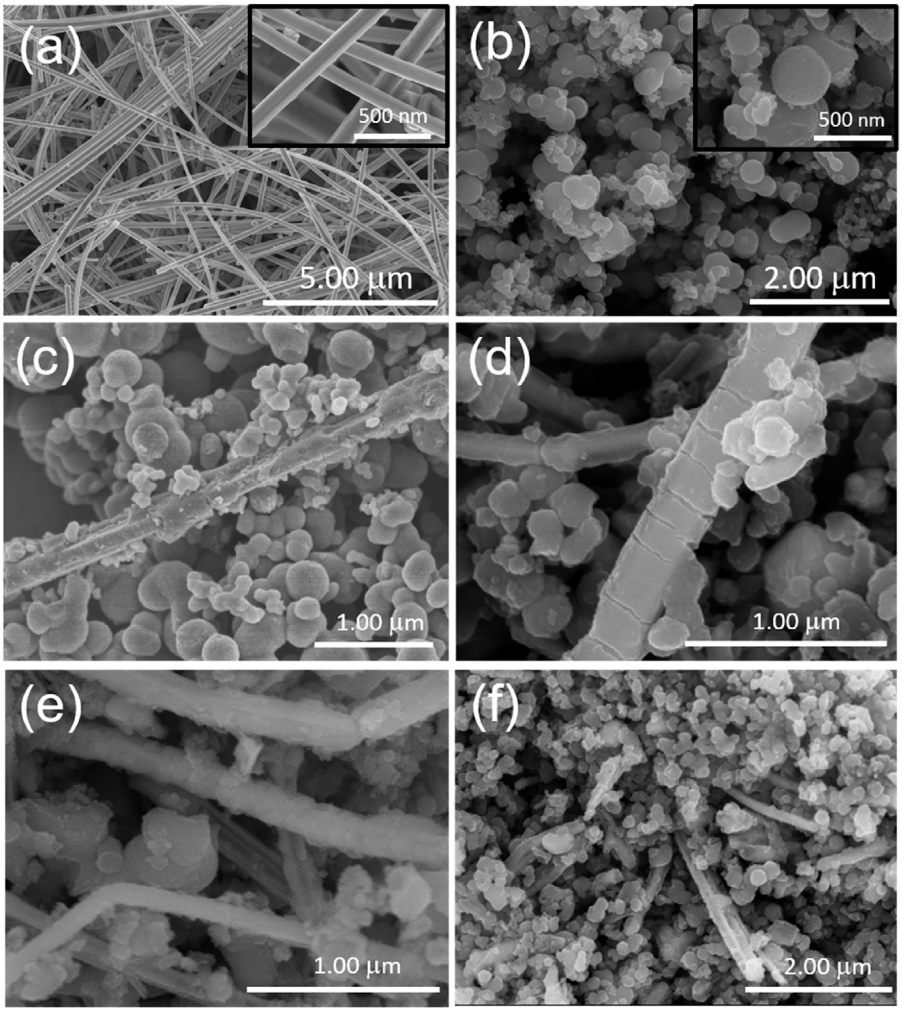

Fig. 1. SEM images of (a) Cu-Ni NWs, (b) TiO_2 NPs, (c) S1, (d) S3, (e) S5 and (f) S20.

data, the contact time of the flowing acetaldehyde gas with the catalysts was calculated to be 9 min. Firstly, the concentration of acetaldehyde gas was reached to adsorption/desorption equilibrium in the reaction system without any light irradiation, and the whole adsorption time was about 125 min. Then the initial concentration of acetaldehyde after adsorption equilibrium was returned to 500 ± 10 ppm for all experiments, which remained constant until a 500 W xenon lamp switched on. The distance between the sample and the lamp was 20 cm. The initial concentration of water vapor was 1.20 ± 0.01 vol%, and the initial temperature was $25 \pm 1\,^{\circ}C$. During the photocatalytic reaction, the acetaldehyde concentration decreased with the light illumination time increase until it reached a stable level. And each reaction lasted for 180 min, the concentration of acetaldehyde gas during the reaction was measured by GC with 5 min intervals. The degradation efficiency of acetaldehyde was calculated as follows:

$$\eta = \frac{C_0 - C}{C_0} \times 100\%$$

Where C was the acetaldehyde concentration at intervals and C_0 was the initial acetaldehyde concentration after the adsorption/desorption equilibrium.

3. Results and discussion

3.1. Characterization of TCN hybrid photocatalysts

The morphologies of the as-prepared Cu-Ni NWs, TiO_2 NPs, and TCN composites (S1, S3, S5, S20) were presented with SEM images (Fig. 1). As shown in Fig. 1a, Cu-Ni NWs (85–115 nm in diameters and 130 μm in length) were clearly observed. Typical TiO_2 NPs shown in Fig. 1b were nearly monodispersed without secondary structure and the diameters were about 250 nm. The size distribution of the TiO_2 NPs was obtained from the SEM images by counting 100 particles. Fig. 1c–f exhibited SEM images of synthetic composites with different ratio of Cu-Ni NWs, 1%, 3%, 5% and 20% respectively. First, TiO_2 NPs and Cu-Ni NWs structures can be observed in all these images and the diameter of nanowires were enlarged apparently because of the TiO_2 outer layer. Second, the amounts of nanowires increased obviously in composites with more Cu-Ni NWs added during the preparation process. Third, the length of nanowires was cut to several micrometers and formed crosslinking topology due to the intense and corrosive TIP hydrothermal reaction process [40].

TEM images were employed to observe the evolution of TCN composite's microstructure. Fig. 2a expressed that Cu-Ni NWs samples were flexible and uniform thickness wires with 110 nm diameter. Meantime, cylindrical surface of the wires could be seen as very smooth. Fig. 2b showed that spherical TiO_2 nanoparti-

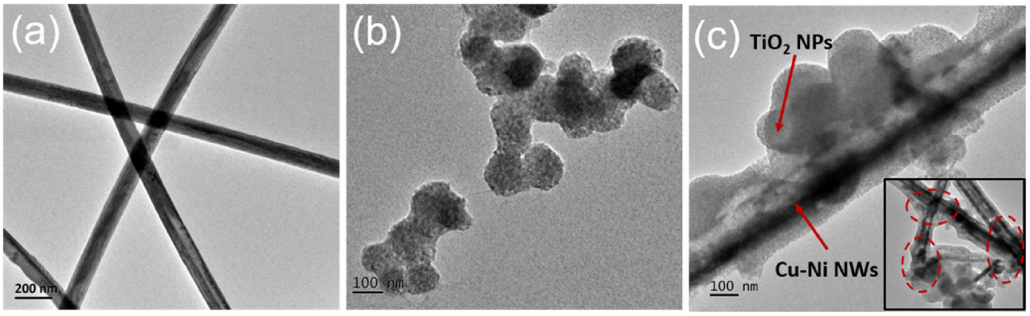

Fig. 2. TEM images of (a) Cu-Ni NWs, (b) TiO_2 NPs, (c) TCN composites.

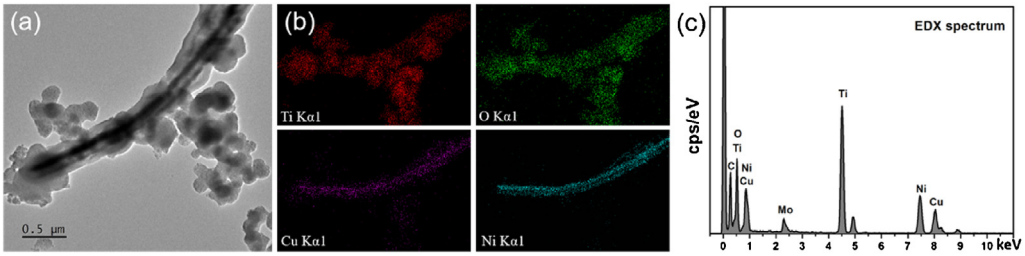

Fig. 3. EDX spectra and elemental mapping of TCN composites, (a) TEM image of TCN composite, (b) EDX elemental mapping images of Ti, O, Cu and Ni respectively, and (c) EDX spectroscopy of TCN composite.

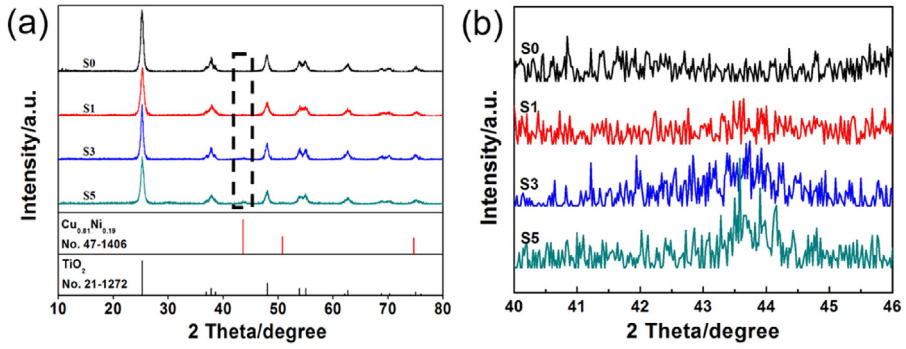

Fig. 4. XRD pattern of pure TiO_2 and TCN composite samples with different Cu-Ni wt%.

cles combined each other with about 200 nm diameter of single particle. Subsequently, TCN composites could be seen clearly in Fig. 2c, compact TiO_2 coating wrapped around the Cu-Ni NWs to form 100–200 nm thickness layer and the surface of composite nanowires became rough compared with the pure Cu-Ni NWs. The inset of Fig. 2c displayed the junction parts of composite wires, different from the well-dispersed Cu-Ni NWs (see Fig. 2a), these wires were connected with each other in the composite matrix because of the welding structures origin from TiO_2 out layer. Furthermore, it also could be found in Fig. 2c that TiO_2 grow into agglomerating spherical-shaped particles except the shell of Cu-Ni NWs, which was thought to coincide with the above SEM results. For further investigating the element distribution of composite wires, EDX analyses were carried out in the observation. Fig. 3 exhibited the EDX spectra and elemental mapping of Ti, O, Cu and Ni in the composites. The results strongly proved that the one-dimensional morphology of Cu-Ni wires were still remained intact after composite synthetic process. Also, TiO_2 parts were observed to grow along with the radial direction of Cu-Ni NWs and wrapped them as a shell based on the images of elemental mapping.

The XRD pattern of the TCN composites was shown in Fig. 4(a). It was obvious that the TCN composites with different weight ratios of Cu-Ni NWs exhibit similar XRD patterns. The pattern indicated that the diffraction peaks center at $2\theta = 43.60^\circ$, 50.79° and 74.67°, which agreed with the (111), (200), and (220) reflections of the phase of $Cu_{0.81}Ni_{0.19}$ (JCPDS No. 47-1406), and the relative intensity of these peaks was strengthened gradually with the ratio of Cu-Ni NWs increasing. The enlarged XRD pattern of Fig. 4(a) between 40° and 46° was presented as Fig. 4(b), in which could be seen clearly that the diffraction peaks of $Cu_{0.81}Ni_{0.19}$ located at 43.60°. And the peak intensity was enhanced with the increasing of Cu-Ni NWs weight ratio. The diffraction peaks center at 25.28°, 37.80°, 48.05°, 53.89°, 55.06°, 62.68°,68.76°, 70.30° and 75.02° could be indexed to the (101), (004), (200), (105), (211), (204), (116), (220), and (215) crystal planes of anatase phase TiO_2 (JCPDS No. 21-1272), respectively. In general, the two sets of diffraction patterns were consistent with $Cu_{0.81}Ni_{0.19}$ and anatase TiO_2, and no peaks for other crystal structures were observed.

Raman spectrum was used to investigate the phase transformation, crystallite size and oxygen vacancy defect of TiO_2 based nanocomposites. The Raman spectra of pure TiO_2, pure Cu-Ni NWs and TCN composite samples were shown in Fig. 5. For the anatase TiO_2, five characteristic peaks of TiO_2 anatase phase approximately at $\lambda = 144$, 197, 396, 517 and 639 cm^{-1} were observed, which correspond to the E_g, E_g, B_{1g}, A_{1g}, and B_{2g} vibrational modes, respectively [41–43]. For Cu-Ni NWs sample, no obvious peak was observed. The

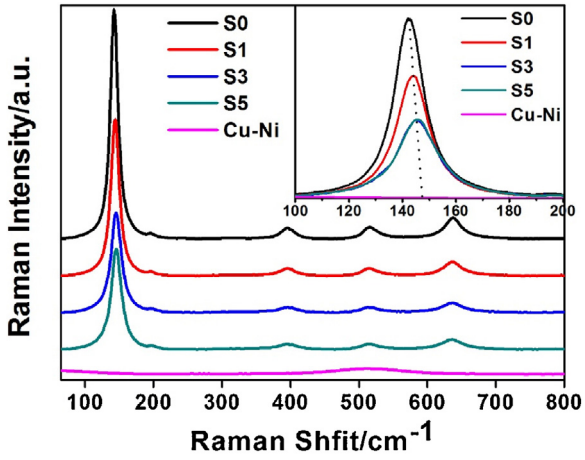

Fig. 5. Raman spectra of pure TiO_2, pure Cu-Ni NWs and TCN composite samples respectively, inset shows corresponding enlarged Raman spectra near E_{1g} vibrational modes.

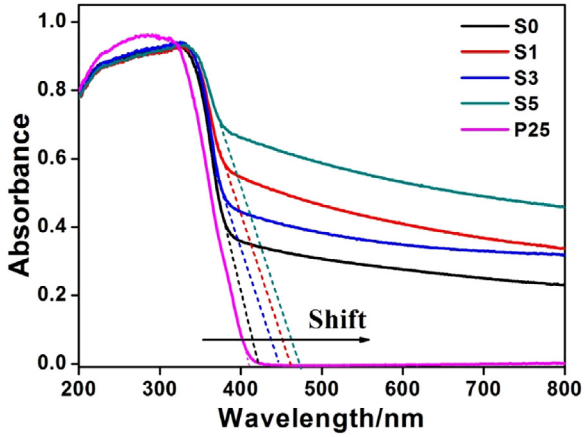

Fig. 6. UV–vis absorption spectra of pure TiO_2 and TCN composite samples.

enlarged Raman spectra at 144 cm^{-1} was presented at the inset of Fig. 5. It could be seen that the most intense peaks of pure TiO_2 sample (S0) appeared at 144 cm^{-1} corresponding to the E_g mode, while 2 cm^{-1} shift toward longer wavenumber to 146 cm^{-1} peak was observed for TCN composites (S1, S3, S5) with small broadening. Besides, the main Raman peaks of S3 and S5 occupied the similar locations. This blue shift in TCN composites was due to the recombination of Cu-Ni NWs over TiO_2 producing a change in the local structure of TiO_2 [44], and the TCN composite caused the lattice distortion or residual stress owing to their lattice mismatch at the interface of Cu-Ni NWs and TiO_2 [45]. The existence of lattice defects was beneficial for the formation of oxygen vacancies, because they could adsorb and activate oxygen, and provided the lattice sites of oxygen migration [46]. In addition, this blue shifts of the Raman band was also in agreement with the results obtained by UV/Vis spectroscopy.

To investigate the optical absorption properties of TCN composite photocatalysts, the UV–visible absorption spectra of TiO_2(P25); contrast pure TiO_2 and TCN composites were examined. As shown in Fig. 6, after Cu-Ni NWs introducing, the light absorption of the nanocomposite was enhanced obviously in visible-light region. The reason could be attributed to the surface plasmon resonance (SPR) effect of Cu-Ni NWs, which was the coherent oscillation of conduction electrons induced by light irradiation [29]. And the change of the refractive index around Cu-Ni core also broadened the light response range of the nanocomposite matrix [47]. Furthermore, the absorption edge of the TCN composites shifted to 450 nm (460 nm, 470 nm) obviously. According to Kubelka–Munk equation, the decrease in the band gap on TCN composites compared to the TiO_2 (P25) was attributed to the electron acceptor character of the Cu-Ni NWs [48]. The redshift of the absorption edge indicated that the TCN composites could facilitate a broader and more efficient utilization of light for photocatalytic reactions.

3.2. Photocatalytic activity measurement

The photocatalytic activities of the TCN composites were evaluated by degradation of flowing acetaldehyde gas both under UV and visible light irradiation. The degradation profiles of the samples with different Cu-Ni NWs weight ratios were shown in Fig. 7. The first 125 min represented the time used for reaching adsorption–desorption equilibrium. The C/C_0 decreased to 0 at the very beginning because acetaldehyde gas was adsorbed completely. The adsorption in this phase included sink effect (on the walls of chamber) and absorption on the surface of TCN samples. With the continuous replenishing acetaldehyde gas into photoreactor, the concentration of acetaldehyde reached to equilibrium, and the ratio of C/C_0 increased to 1 again. After reaching equilibrium, the light was turned on and the photocatalytic reactions was started. From Fig. 7(a), It could be found that all the samples exhibit excellent photocatalytic activities and S3 exhibits the highest photocatalytic activity, the degradation rate under UV light was about 88%. It was noted that in the absence of Cu-Ni NWs, acetaldehyde was degraded about 40% with S0. In order to optimize the weight ratio of Cu-Ni NWs on the nanocomposite system's photocatalytic activities, five sets of photocatalysts with various Cu-Ni NWs weight ratios (S1 = 1 wt%, S3 = 3 wt%, S5 = 5 wt%, and S20 = 20 wt%) were also detected in this work. The results showed that the photocatalytic activities were 76% for S1, 65% for S5, and 56% for S20, respectively, which were all lower than 88% for S3. It indicated that photocatalytic activity of the samples was enhanced with the weight ratio of Cu-Ni NWs increased until reach to 3 wt%. However, when the weight ratio continue increased to over 3 wt%, the photocatalytic activity of the samples began to decline. This decline could be explained that higher Cu-Ni NWs contents might cause more reflection of light irradiation and recombination of electron-hole pairs. According to experimental measurement, pure Cu-Ni NWs doesn't possess photocatalytic performance for the degradation of acetaldehyde. Therefore, 3 wt% addition of Cu-Ni NWs might be the optimal proportion for the acetaldehyde photodegradation in these TCN samples. In addition, the TCN samples displayed absorption in the visible-light region based on the UV–vis absorption spectra. As shown in Fig. 7(b), it could be found that S3 sample also exhibited the highest photocatalytic activity, 56% degradation efficiency under visible light irradiation, which was higher than S1, S5 and S20. The excellent visible light catalytic activity of S3 sample matched well with its visible light response in UV–visible absorption spectra (Fig. 6), which indicated that the TCN's light absorption was improved obviously in the visible-light region and the light response range extended at the same time.

The reason of the TCN's excellent photocatalytic performance could be attributed to the existence of Cu-Ni NWs. Conductive Cu-Ni NWs served as electron reservoirs to suppress the recombination of electron–hole pairs of TiO_2 and thus promote the reaction process. The schematic diagram of the TCN composites was demonstrated in Fig. 9. The excited electrons in CB of TiO_2 were immediately transferred to Cu-Ni NWs and participated in reduction process. In the same time, due to the gathering of photo-generated electrons in Cu-Ni NWs, the recombination rate of electron-hole pairs decreased, so more holes at the VB of TiO_2 could participate in the process of oxidation reaction. In addition, the photocatalytic activity of the TCN composite photocatalysts prepared

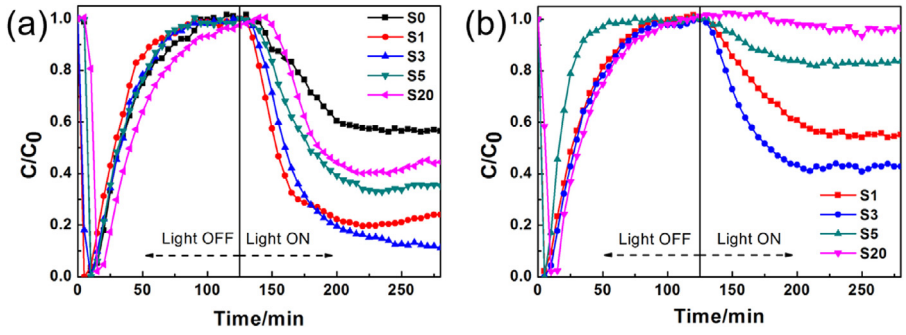

Fig. 7. Comparison of the photocatalytic degradation of flowing acetaldehyde gas between pure TiO_2 and TCN composite samples under (a) UV light and (b) visible light, respectively.

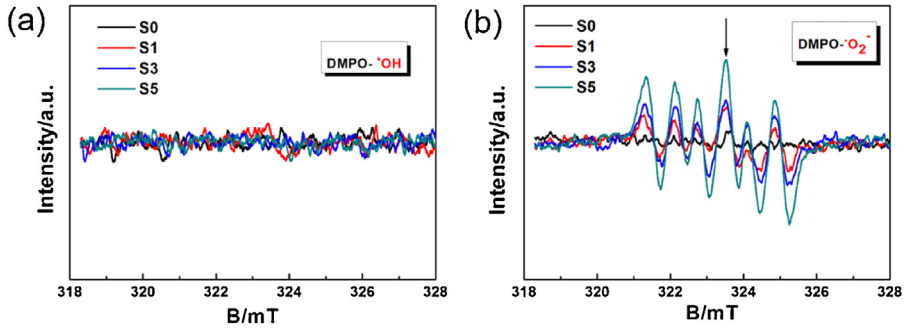

Fig. 8. DMPO spin-trapping ESR spectra under visible light irradiation (λ > 420 nm) for 15 min in aqueous solutions (a) and ethanol solutions (b), respectively.

by this method was chemically stable, every sample was tested for more than four hours in sustained photocatalytic reaction and still remained photocatalytical active. From the above results, it could be concluded that the TCN composites were able to degrade flowing CH_3CHO gas effectively.

Comparing to S0 and S1 samples, S3 possessed better photodegradation efficiency because it was able to provide sufficient one dimensional electron pathways in the matrix and then inhibit the recombination of photo generated electron-hole pair. Nevertheless, when the weight ratio of Cu-Ni NWs was in the range of 3–20%, the photodegradation efficiency on flowing acetaldehyde gas would decrease with the Cu-Ni NWs content increased. It was considered that too much bimetallic nanowires covered most surface of TiO_2, causing extreme reflections of light irradiation. As a result, photocatalytic performance of the TCN composites would be depressed due to the reductions of light energy utilization [31]. At the same time, excess Cu-Ni NWs would become the recombination center and affect its own charge separation abilities [30,31,45].

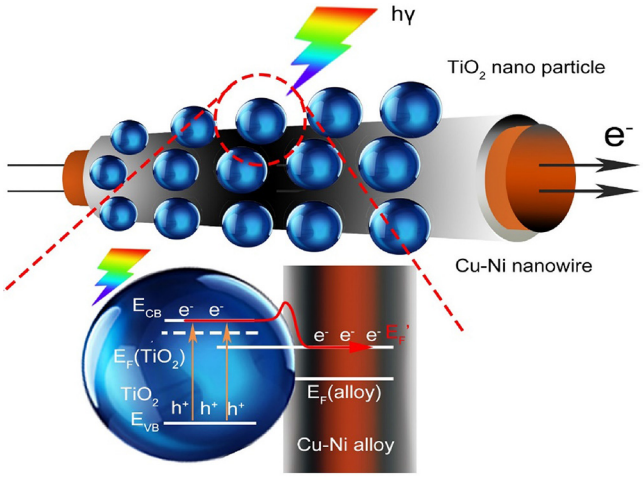

Fig. 9. Schematic and photocatalytic mechanism diagram of TCN heterostructure. $E_F(TiO_2)$ and E_F' refer to the Fermi levels of TiO_2 before and after attaining equilibrium, E_F(alloy) represents the Fermi levels of Cu-Ni NWs alloy.

3.3. DMPO spin-trapping ESR spectrum

Reactive species, such as superoxide radical ($\bullet O_2^-$), electron holes (h^+), and hydroxyl radicals ($\bullet OH$), had been identified to perform vital functions in the photocatalytic degradation process [49]. In this work, DMPO spin-trapping ESR spectrum was used to study the effect of Cu-Ni NWs modification on the formation of $\bullet OH$ and $\bullet O_2^-$ radicals for this TCN composite system.

It could be seen from Fig. 8a that negligible signals for $\bullet OH$ radicals could be detected for all the samples. According to the analyses, it was found that the potential of the photo-generated hole in the VB of TiO_2 was not higher enough to oxidize H_2O and produce $\bullet OH$ radicals ($E_0(-OH/\bullet OH) = 2.4$ V) [50,51]. Thus it was understandable that the signals of $\bullet OH$ radicals in these samples were hardly measured under visible light irradiation. However, the DMPO–ESR analysis results revealed that the signal of $\bullet O_2^-$ radicals was noticeably enhanced after the incorporation of Cu-Ni NWs on TiO_2, and the $\bullet O_2^-$ radical signals of these samples were also gradually improved with the weight ratio of Cu-Ni NWs increased (Fig. 8b). The much more generated $\bullet O_2^-$ radicals should be benefit from the enhanced charge separation and by reducing the O_2 through the separated electrons, while the production of $\bullet OH$ was inhibited.

The intensity of the $\bullet O_2^-$ radicals signal on the respective catalysts (Fig. 8b) was consistent with the photocatalytic activity under visible light irradiation. These data suggested that the electron transfer from photoactivated TiO_2 nanoparticles to bimetallic nanowires was one of the crucial factors influencing the photo-

catalytic activity. The TCN composite catalysts promoted electron transfer efficiently and exhibited high photocatalytic activity.

3.4. Photocatalytic mechanism of TCN heterostructure

Based on the experimental results, a possible schematic elaboration of photocatalytic mechanism upon TCN heterostructure was proposed to explain the reason why TCN composites exhibited excellent photocatalytic activity.

Firstly, the incorporation of Cu-Ni NWs improved the light-harvesting ability of TiO_2 ranging from UV to visible light as demonstrated in UV–vis absorption spectra (Fig. 6), which favored the production of more photo-generated electron-hole pairs on the TiO_2 surface. Based on the theory of optical band structure of pure TiO_2 and as-prepared Cu-Ni NWs samples in previous work, Fig. 9 showed a possible energy band diagram to explain the process, the direct coupling of Cu-Ni NWs and TiO_2 caused the Fermi level to equilibrate, and attained an energy level close to the conduction band of the TiO_2 semiconductor. As shown in Fig. 9, when there had light illuminate on the TCN composites, the generated electron–hole pairs could be separated into electrons and holes, while electrons could transfer into the Cu-Ni NWs and holes would located on the VB of TiO_2 nanoparticles, respectively.

Secondly, a built-in electric field induced by the SPR effect of bimetallic nanowires would accelerate the photo-generated electrons and holes separation. The Schottky barrier created at the Cu-Ni NWs/TiO_2 heterojunction interface could be estimated to be 0.85–1.35 eV, for the work functions of Cu and Ni were 4.65 eV (Φ_{Cu} = 4.65 eV) and 5.15eV(Φ_{Ni} = 5.15 eV) [38] respectively, the electron affinity of TiO_2 conduction band was 3.8 eV (X_{TiO2} = 3.8 eV) [39]. And the work function of bimetal was expressed by the sum of the work functions of two metal components [52,53], thus the work function of $Cu_{1-x}Ni_x$ bimetal could be expressed as follows:

$$W_{alloy}\,(\mathrm{eV}) = (1 - \mathrm{x}) \cdot W_{Cu} + \mathrm{x} \cdot W_{Ni}$$

The estimated value of the Schottky barrier height in this system was similar to the Cu-Pt/TiO_2 heterojunction system [44]. The higher barrier at Cu-Ni NWs/TiO_2 heterojunction could prevent electrons from recombining with holes again, because more energy would be needed for the electron migration. On the one hand, a suitable Schottky barrier could enhance electron–hole separation so that increase the lifetime of charge carriers. On the other hand, the strong confinement and anisotropic effect in this one dimension bimetal/semiconductor heterostructure could accelerate the transfer of electrons and holes over the TCN matrix.

Thirdly, the conductive Cu-Ni NWs would perform as electron traps to further facilitate the separation of photo-generated electron–hole pairs. After the separation of electrons and holes, these two kinds of photo-generated charge carriers would be transformed into active species (•OH) subsequently which were responsible for the degradation of pollutants. In particular, the separated electrons would reduce O_2 to $^{\bullet}O_2^-$, and the produced $^{\bullet}O_2^-$ could also combine with protons to yield HOO• and then H_2O_2 to oxidize pollutants [50]. Meanwhile the formed H_2O_2 could be further transformed into •OH afterward by trapping electrons. Furthermore, the enrichment of electrons on the Cu-Ni NWs could facilitate their participation in the multiple-electron reduction reaction of oxygen [51]. Simultaneously, the concentration of h^+ on TiO_2 could also improve the photocatalytic reaction rates of acetaldehyde degradation. As known, the first step reaction was crucial for determining the reaction rate and the production ratio in multistep continuous reactions ($O_2 \rightarrow {}^{\bullet}O_2^- \rightarrow H_2O_2 \rightarrow {}^{\bullet}OH$) [54]. Thus, more $^{\bullet}O_2^-$ radicals were produced in this photocatalytic system than •OH generation, given that $^{\bullet}O_2^-$ radicals were major reactive oxidation species, this matched well with the ESR results.

The above theoretical analysis proved that the photocatalytic performance of TCN composite benefits from the optimized optical band gap, moderate Schottky barrier height, good metal conductivity properties and structure of band alignment in the heterostructure photocatalyst system.

4. Conclusions

In summary, Cu-Ni bimetallic nanowires were introduced into TiO_2 matrix by one-step hydrolysis approach. The photocatalytic performance of composites were evaluated using high concentration flowing acetaldehyde gas pollutant. The results indicated that the highest photodegradation efficiency among all the samples was obtained as 88% and 56% under UV and visible light, respectively. The 3 wt% addition of Cu-Ni NWs was proved to be an optimal proportion for the acetaldehyde photodegradation in these TCN samples. Based on the ESR analyze, this new heterostructured photocatalyst succeed in not only utilizing both visible and UV light but also enhancing photo-generated charge separation capability. The reasons might be attribute to the one-dimensional electron pathways, surface plasmon resonance effects and modified bimetallic Schottky barrier. This work might help to clarify the photon-generated carrier separation and transmission processes in metal-semiconductor network topology, and provide an effective method for the preparation of bimetal-based heterostructured photocatalysts. Furthermore, as an effective photocatalytic material, the optimized TCN composites also could be used in eliminating VOCs in environment and applied in air cleaner to remove indoor harmful gaseous pollution.

Notes

The authors declare no competing financial interest.

Acknowledgements

This work was financially supported by the National Key Research and Development Program of China (2016YFA0203000), the Key Project of International Cooperation of the Chinese Academy of Sciences (GJHZ1656), Strategic Cooperation Project of Chinese Academy of Sciences and Guangdong Government (2013B091100002).

References

[1] U. Schlink, et al., A framework to interpret passively sampled indoor-air VOC concentrations in health studies, Build. Environ. 105 (2016) 198–209.
[2] R.K. Nath, M.F.M. Zain, M. Jamil, An environment-friendly solution for indoor air purification by using renewable photocatalysts in concrete: a review, Renew. Sustain. Energy Rev. 62 (2016) 1184–1194.
[3] F.L. Carazo, et al., Indoor air contaminants and their impact on respiratory pathologies, Arch. Bronconeumol. 49 (1) (2013) 22–27.
[4] X. Shen, et al., Heterogeneous reactions of volatile organic compounds in the atmosphere, Atmos. Environ. 68 (2013) 297–314.
[5] N.L. Ng, et al., Secondary organic aerosol formation from m-xylene, toluene, and benzene, Atmos. Chem. Phys. 7 (14) (2007) 3909–3922.
[6] M.A. Sidheswaran, et al., Energy efficient indoor VOC air cleaning with activated carbon fiber (ACF) filters, Build. Environ. 47 (2012) 357–367.
[7] S. Wang, H.M. Ang, M.O. Tade, Volatile organic compounds in indoor environment and photocatalytic oxidation: state of the art, Environ. Int. 33 (5) (2007) 694–705.
[8] V. Demidiouk, S.I. Moon, J.O. Chae, Toluene and butyl acetate removal from air by plasma-catalytic system, Catal. Commun. 4 (2) (2003) 51–56.
[9] C.S. Lu, M.R. Lin, I.H. Wey, Removal of pentane and styrene mixtures from waste gases by a trickle-bed air biofilter, J. Chem. Technol. Biotechnol. 76 (8) (2001) 820–826.
[10] A.Y. Chen, et al., Effect of annealing atmosphere on the thermal coarsening of nanoporous gold films, Appl. Surf. Sci. 355 (2015) 133–138.
[11] M.R. Hoffmann, et al., Environmental applications of semiconductor photocatalysis, Chem. Rev. 95 (1) (1995) 69–96.

[12] A. Fujishima, X. Zhang, D. Tryk, Heterogeneous photocatalysis: from water photolysis to applications in environmental cleanup, Int. J. Hydrogen Energy 32 (14) (2007) 2664–2672.
[13] T. Ochiai, A. Fujishima, Photoelectrochemical properties of TiO2 photocatalyst and its applications for environmental purification, J. Photochem. Photobiol. C Photochem. Rev. 13 (4) (2012) 247–262.
[14] N. Zhang, et al., CdS–graphene nanocomposites as visible light photocatalyst for redox reactions in water: a green route for selective transformation and environmental remediation, J. Catal. 303 (2013) 60–69.
[15] C. Zhao, et al., UV and visible light activated TiO2 photocatalysis of 6-hydroxymethyl uracil, a model compound for the potent cyanotoxin cylindrospermopsin, Catal. Today 224 (2014) 70–76.
[16] A.Y. Chen, et al., Microstructure and electrocatalytic performance of nanoporous gold foils decorated by TiO2 coatings, Surf. Coat. Technol. 286 (2016) 113–118.
[17] J. Schneider, et al., Understanding TiO2 photocatalysis: mechanisms and materials, Chem. Rev. 114 (19) (2014) 9919–9986.
[18] R. Daghrir, P. Drogui, D. Robert, Modified TiO2 for environmental photocatalytic applications: a review, Ind. Eng. Chem. Res. 52 (10) (2013) 3581–3599.
[19] G. Liu, et al., Synergistic effects of B/N doping on the visible-light photocatalytic activity of mesoporous TiO2, Angew. Chem. Int. Ed. Engl. 47 (24) (2008) 4516–4520.
[20] D. Yang, et al., Synthesis of Ag/TiO2 nanotube heterojunction with improved visible-light photocatalytic performance inspired by bioadhesion, J. Phys. Chem. C 119 (11) (2015) 5827–5835.
[21] N. Seriani, C. Pinilla, Y. Crespo, Presence of gap states at Cu/TiO2 anatase surfaces: consequences for the photocatalytic activity, J. Phys. Chem. C 119 (12) (2015) 6696–6702.
[22] J.S. Lee, K.H. You, C.B. Park, Highly photoactive, low bandgap TiO2 nanoparticles wrapped by graphene, Adv. Mater. 24 (8) (2012) 1084–1088.
[23] B. Qiu, M. Xing, J. Zhang, Mesoporous TiO2 nanocrystals grown in situ on graphene aerogels for high photocatalysis and lithium-ion batteries, J. Am. Chem. Soc. 136 (16) (2014) 5852–5855.
[24] W. Zhao, et al., Synthesis, characterization, and photocatalytic properties of SnO2/rutile TiO2/anatase TiO2 heterojunctions modified by Pt, J. Phys. Chem. C 118 (40) (2014) 23117–23125.
[25] Y.-C. Pu, et al., Au nanostructure-decorated TiO2 nanowires exhibiting photoactivity across entire UV-visible region for photoelectrochemical water splitting, Nano Lett. 13 (8) (2013) 3817–3823.
[26] Z. Zhao, et al., The study of microstructure, optical and photocatalytic properties of nanoparticles(NPs)-Cu/TiO2 films deposited by magnetron sputtering, J. Alloys Comp. 652 (2015) 307–312.
[27] C.-Y. Tsai, Preparation of Cu-doped TiO2 photocatalyst with thermal plasma torch for low-concentration mercury removal, Aerosol Air Qual. Res. 13 (2) (2013) 639–648.
[28] T. Montini, et al., Nanostructured Cu/TiO2 photocatalysts for H2 production from ethanol and glycerol aqueous solutions, ChemCatChem 3 (3) (2011) 574–577.
[29] B. Babu, et al., Facile synthesis of Cu@TiO2 core shell nanowires for efficient photocatalysis, Mater. Lett. 176 (2016) 265–269.
[30] Y. Zhang, et al., Decoration of Cu nanowires with chemically modified TiO2 nanoparticles for their improved photocatalytic performance, J. Mater. Sci. 48 (19) (2013) 6728–6736.
[31] C. Jia, H.-S. Chen, P. Yang, Selective growth of TiO2 beads on Ag nanowires and their photocatalytic performance, CrystEngComm 17 (26) (2015) 4895–4902.
[32] L. Shi, et al., A long-term oxidation barrier for copper nanowires: graphene says yes, Phys. Chem. Chem. Phys. 17 (6) (2015) 4231–4236.
[33] H. Zhai, et al., Transparent heaters based on highly stable Cu nanowire films, Nano Res. 9 (12) (2016) 3924–3936.
[34] X. Wang, et al., Synthesis of metal/bimetal nanowires and their applications as flexible transparent electrodes, Small 11 (36) (2015) 4737–4744.
[35] Y. Shiraishi, et al., Pt-Cu bimetallic alloy nanoparticles supported on anatase TiO2: highly active catalysts for aerobic oxidation driven by visible light, ACS Nano 7 (10) (2013) 9287–9297.
[36] T. Tanabe, et al., Site-selective deposition of binary Pt–Pb alloy nanoparticles on TiO2 nanorod for acetic acid oxidative decomposition, J. Catal. 340 (2016) 276–286.
[37] D. Tsukamoto, et al., Photocatalytic H2O2 production from ethanol/O2 system using TiO2 loaded with Au–Ag bimetallic alloy nanoparticles, ACS Catal. 2 (4) (2012) 599–603.
[38] H.B. Michaelson, The work function of the elements and its periodicity, J. Appl. Phys. 48 (11) (1977) 4729–4733.
[39] N. Tokmoldin, et al., A hybrid inorganic-organic semiconductor light-emitting diode using ZrO2 as an electron-injection layer, Adv. Mater. 21 (34) (2009) 3475–3478.
[40] D.P. Langley, et al., Metallic nanowire networks: effects of thermal annealing on electrical resistance, Nanoscale 6 (22) (2014) 13535–13543.
[41] B. Karunagaran, et al., Structural, optical and Raman scattering studies on DC magnetron sputtered titanium dioxide thin films, Sol. Energy Mater. Sol. Cells 88 (2) (2005) 199–208.
[42] Y. Su, J. Yu, J. Lin, Vapor-thermal preparation of highly crystallized TiO2 powder and its photocatalytic activity, J. Solid State Chem. 180 (7) (2007) 2080–2087.
[43] J. Yu, et al., Effects of pH on the microstructures and photocatalytic activity of mesoporous nanocrystalline titania powders prepared via hydrothermal method, J. Mol. Catal. A Chem. 258 (1–2) (2006) 104–112.
[44] S. Farsinezhad, H. Sharma, K. Shankar, Interfacial band alignment for photocatalytic charge separation in TiO2 nanotube arrays coated with CuPt nanoparticles, Phys. Chem. Chem. Phys. 17 (44) (2015) 29723–29733.
[45] C. Jia, et al., Photocatalytic activity evolution of different morphological TiO2 shells on Ag nanowires, ChemCatChem 8 (4) (2016) 839–847.
[46] B. Bai, J. Li, Positive effects of K+ions on three-dimensional mesoporous Ag/Co3O4 catalyst for HCHO oxidation, ACS Catal. 4 (8) (2014) 2753–2762.
[47] Y. Zhao, et al., The structure, morphology, and the metal-enhanced fluorescence of nano-Ag/ZnO core–shell structure, Appl. Nanosci. 5 (5) (2014) 521–525.
[48] N. Riaz, et al., Photodegradation of Orange II under visible light using Cu-Ni/TiO2: influence of Cu:Ni mass composition, preparation, and calcination temperature, Ind. Eng. Chem. Res. 52 (12) (2013) 4491–4503.
[49] Y. Li, et al., Hybridization of rutile TiO2 (rTiO2) with g-C3N4 quantum dots (CN QDs): an efficient visible-light-driven Z-scheme hybridized photocatalyst, Appl. Catal. B Environ. 202 (2017) 611–619.
[50] S. Zhao, et al., g-C3N4/TiO2 hybrid photocatalyst with wide absorption wavelength range and effective photogenerated charge separation, Sep. Purif. Technol. 99 (2012) 50–54.
[51] F. Dong, et al., An advanced semimetal-organic Bi spheres-g-C3N4 nanohybrid with SPR-enhanced visible-light photocatalytic performance for NO purification, Environ. Sci. Technol. 49 (20) (2015) 12432–12440.
[52] R. Ishii, et al., Work function of binary alloys, Appl. Surf. Sci. 169–170 (3) (2001) 658–661.
[53] I. Pašti, S. Mentus, Electronic properties of the PtxMe1–x/Pt(111) (Me = Au, Bi, In, Pb, Pd, Sn and Cu) surface alloys: DFT study, Mater. Chem. Phys. 116 (1) (2009) 94–101.
[54] R.N. Perham, Swinging arms and swinging domains in multifunctional enzymes: catalytic machines for multistep reactions, Annu. Rev. Biochem. 69 (69) (2000) 961–1004.